



Showcasing research from Dr Ke's laboratory, College of Chemistry and Chemical Engineering, Anhui University of Technology, Maanshan, Anhui, P. R. China.

Spontaneous generation of singlet oxygen on microemulsion-derived manganese oxides with rich oxygen vacancies for efficient aerobic oxidation

N_{55} - MnO_2 nanocatalysts with oxygen vacancy concentrations as high as 51.1% can be obtained by strategically incorporating defect engineering and interstitial N using compartmentalized-microemulsion crystallization followed by post-calcination. This feature allows the nanocatalyst to expose a substantial number of O_v and interstitial N sites on the surface of N_{55} - MnO_2 , facilitating effective chemisorption and activation of O_2 . As a result, the N_{55} - MnO_2 nanocatalyst enables room-temperature aerobic oxidation of alcohols with a yield surpassing 99%, representing a 6.7-fold activity enhancement compared to ϵ - MnO_2 without N-doping.

As featured in:



See Chao Wan, Qingping Ke, Yunqing Kang, Yusuke Yamauchi *et al.*, *Chem. Sci.*, 2023, 14, 13402.

Cite this: *Chem. Sci.*, 2023, 14, 13402 All publication charges for this article have been paid for by the Royal Society of Chemistry

Spontaneous generation of singlet oxygen on microemulsion-derived manganese oxides with rich oxygen vacancies for efficient aerobic oxidation†

Jun Tang,^{ab} Junbao Chen,^a Zhanyu Zhang,^a Qincheng Ma,^a Xiaolong Hu,^a Peng Li,^a Zhiqiang Liu,^a Peixin Cui,^c Chao Wan,^{*de} Qingping Ke,^{*a} Lei Fu,^e Jeonghun Kim,^f Takashi Hamada,^g Yunqing Kang^{*e} and Yusuke Yamauchi^{*fgh}

Developing innovative catalysts for efficiently activating O₂ into singlet oxygen (¹O₂) is a cutting-edge field with the potential to revolutionize green chemical synthesis. Despite its potential, practical implementation remains a significant challenge. In this study, we design a series of nitrogen (N)-doped manganese oxides (N_y-MnO₂, where y represents the molar amount of the N precursor used) nanocatalysts using compartmentalized-microemulsion crystallization followed by post-calcination. These nanocatalysts demonstrate the remarkable ability to directly produce ¹O₂ at room temperature without the external fields. By strategically incorporating defect engineering and interstitial N, the concentration of surface oxygen atoms (O_s) in the vicinity of oxygen vacancy (O_v) reaches 51.1% for the N₅₅-MnO₂ nanocatalyst. This feature allows the nanocatalyst to expose a substantial number of O_v and interstitial N sites on the surface of N₅₅-MnO₂, facilitating effective chemisorption and activation of O₂. Verified through electron paramagnetic resonance spectroscopy and reactive oxygen species trapping experiments, the spontaneous generation of ¹O₂, even in the absence of light, underscores its crucial role in aerobic oxidation. Density functional theory calculations reveal that an increased O_v content and N doping significantly reduce the adsorption energy, thereby promoting chemisorption and excitation of O₂. Consequently, the optimized N₅₅-MnO₂ nanocatalyst enables room-temperature aerobic oxidation of alcohols with a yield surpassing 99%, representing a 6.7-fold activity enhancement compared to ε-MnO₂ without N-doping. Furthermore, N₅₅-MnO₂ demonstrates exceptional recyclability for the aerobic oxidative conversion of benzyl alcohol over ten cycles. This study introduces an approach to spontaneously activate O₂ for the green synthesis of fine chemicals.

Received 23rd August 2023
Accepted 9th October 2023

DOI: 10.1039/d3sc04418a

rsc.li/chemical-science

^aCollege of Chemistry and Chemical Engineering, Anhui University of Technology, Maanshan 243002, Anhui, P. R. China. E-mail: Qingke@ahut.edu.cn^bSchool of Chemistry and Chemical Engineering, Shanxi University, Taiyuan 030006, P. R. China^cKey Laboratory of Soil Environment and Pollution Remediation, Institute of Soil Science, The Chinese Academy of Sciences, Nanjing 210008, P. R. China^dCollege of Chemical and Biological Engineering, Zhejiang University, Hangzhou 310058, P. R. China. E-mail: wanchao@zju.edu.cn^eResearch Center for Materials Nanoarchitectonics (MANA), National Institute for Materials Science (NIMS), 1-1 Namiki, Tsukuba, Ibaraki 305-0044, Japan. E-mail: yqkang@toki.waseda.jp^fDepartment of Chemical and Biomolecular Engineering, Yonsei University, 50 Yonsei-ro, Seodaemun-gu, Seoul 03722, South Korea^gDepartment of Materials Process Engineering, Graduate School of Engineering, Nagoya University, Nagoya 464-8603, Japan^hAustralian Institute for Bioengineering and Nanotechnology (AIBN), The University of Queensland, Brisbane, Queensland 4072, Australia. E-mail: y.yamauchi@uq.edu.au† Electronic supplementary information (ESI) available. See DOI: <https://doi.org/10.1039/d3sc04418a>

Introduction

Singlet oxygen (¹O₂), recognized as a highly active and environmentally friendly reactive oxygen species (ROS), has garnered substantial attention from researchers in recent years.¹⁻⁴ Benefiting from its remarkable oxidative capabilities and eco-friendliness, ¹O₂ has found widespread applications in green catalysis,⁵⁻⁷ photocatalytic degradation,⁸ tumor diagnosis and treatment,⁹ and fluorescence probes.¹⁰ Nevertheless, the practical generation of ¹O₂ typically necessitates intense photoexcitation due to the spin transition between ground and excited state molecular oxygen.¹¹ Throughout the last few decades, a range of photosensitizers, including photosensitive organic dyes,¹² organometallic complexes,¹³ and noble metals,^{14,15} have been devised to produce ¹O₂ by harnessing photogenerated excitons and energy transfer pathways. However, the scarcity of noble metals and the susceptibility of organic photosensitizers to degradation render them inadequate to fulfill the escalating



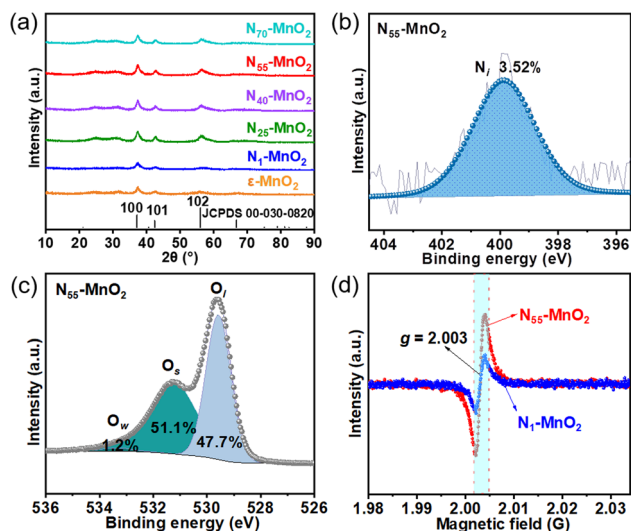


Fig. 1 (a) XRD patterns of N_y -MnO₂ ($y = 1, 25, 40, 55, 70$) and ϵ -MnO₂; (b) N 1s and (c) O 1s XPS spectra of N_{55} -MnO₂ (O_w : oxygen from water adsorption); (d) EPR spectra of N_1 -MnO₂ and N_{55} -MnO₂.

at interstitial sites.³⁵ The introduction of interstitial N minimizes the formation energy of O_v and facilitates the generation of high-concentration O_v .³⁵ As a result, the N_{55} -MnO₂ catalyst, with an optimal interstitial N content, achieves a maximum concentration of surface oxygen atoms (O_s) at 51.1% in the vicinity of O_v (Fig. 1c, S3, and Table S1†).^{36,37} In addition, the O_s content and the unsaturated Mn coordination (Mn^{3+}/Mn^{4+} ratio of 0.90, as shown in Fig. S4†), in N_{55} -MnO₂, significantly exceed that of similar catalysts (Table S2†).^{37–41} Furthermore, the evolutionary trend facilitated by interstitial N-doping is reflected in the increased-intensity peak of O_v at $g = 2.003$ in the electron paramagnetic resonance (EPR) spectrum in Fig. 1d. However, excessive N-doping in N_{70} -MnO₂ tends to occupy the formed vacancies, negatively affecting O_v formation (Fig. S3e†). As observed by transmission electron microscopy (TEM) in Fig. 2a, the N_{55} -MnO₂ catalyst possesses a size of ~ 115 nm, which is consistent with the results from dynamic light scattering (DLS,

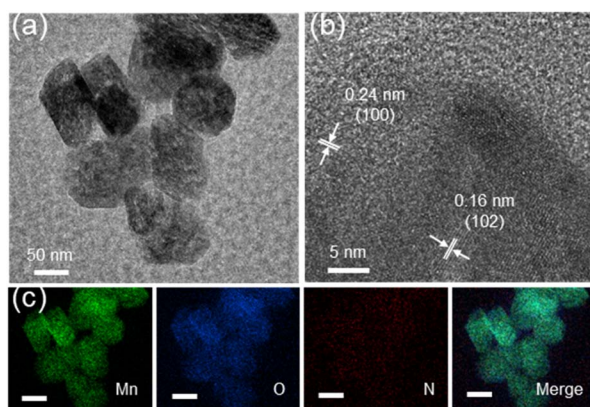


Fig. 2 (a)TEM, (b) HRTEM, and (c) EDS elemental mapping images (scale bars, 50 nm) of N_{55} -MnO₂ nanocatalyst.

Fig. S1c†). This demonstrates the distinctive compartmentalization effect of microemulsions in synthesizing uniform-size nanocatalysts. Additionally, High-resolution TEM (HRTEM) image of N_{55} -MnO₂ reveals d -spacings of 0.24 nm and 0.16 nm (Fig. 2b), corresponding to the (100) and (102) facets, respectively, of ϵ -MnO₂.⁴² Energy dispersive spectroscopy (EDS) element mapping images of N_{55} -MnO₂ demonstrate that interstitial N is uniformly embedded in the MnO₂ lattice (Fig. 2c). Doping interstitial N into MnO₂ leads to alterations in the original electronic structure and unsaturated coordination environment, thus enhancing the catalytic oxidation capacity.³⁷ This is confirmed through hydrogen temperature-programmed reduction (H_2 -TPR), with N_{55} -MnO₂ displaying the most prominent redox capability (Fig. S1d†), consistent with previous reports.^{37,43–47} Additionally, Brunauer-Emmett-Teller (BET) analysis of N_2 adsorption-desorption measurements was conducted to assess the BET parameters of N_y -MnO₂. As shown in Fig. S5 and Table S3,† N_{55} -MnO₂ exhibits the highest BET surface area of 78.7 m² g⁻¹ among the N_y -MnO₂ samples and an average mesopore size of 11.41 nm. This can be attributed to the presence of O_v in N_y -MnO₂, which contribute to the formation of abundant mesopores on the surface of N_y -MnO₂.⁴⁸

Adsorption of O₂ and production of ¹O₂

Previous studies have demonstrated that an increased concentration of O_v enhances the chemical adsorption of O₂, leading to the elongation of the O–O bond and facilitating O₂ activation.^{24,25,48} Our DFT calculations reveal that the adsorption energy of O₂ on the surface of ϵ -MnO₂ is -1.24 eV, whereas it decreases to -2.18 eV on N_{55} -MnO₂ (Fig. 3a). This indicates that the augmented O_v resulting from N-doping reduces the adsorption energy of O₂, thereby promoting its chemisorption and excitation.²⁵ To gain further insights, we employed *in situ* IR spectroscopy for real-time monitoring of O₂ adsorption and activation on the surface of N_{55} -MnO₂. As shown in Fig. 3b, a chemisorption peak of O₂ emerges at 1401 cm⁻¹ in an O₂ atmosphere, followed by the gradual formation of a robust band corresponding to surface-bonded superoxide anion species ($O_2^{\cdot-}$) at 1052 cm⁻¹.^{49,50} This illustrates the role of O_v in promoting O₂ activation. Conversely, no discernible peaks are observed under an O₂ + H₂O vapor atmosphere, possibly due to H₂O occupying the O_v and preventing O₂ adsorption (Fig. S6a†).

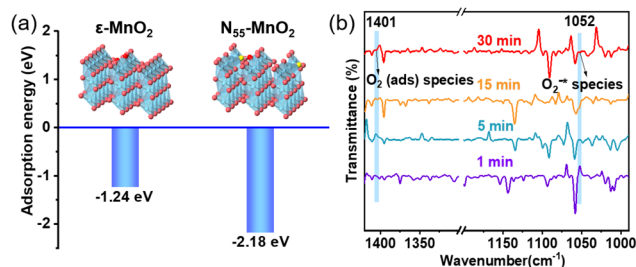


Fig. 3 (a) Adsorption energy of O₂ on the surface of pristine ϵ -MnO₂ and N_{55} -MnO₂ obtained by DFT calculation; (b) *in situ* IR spectra of O₂ adsorbed onto the surface of N_{55} -MnO₂.

The direct interactions between O_2 and N_y - MnO_2 were investigated without light irradiation using EPR. 2,2,6,6-tetramethylpiperidine (TEMP) was employed as a quencher to capture 1O_2 activated by N_y - MnO_2 at room temperature. As depicted in Fig. 4a and b, N_1 - MnO_2 , which exhibits fewer O_v , generates only $^{\bullet}O_2^-$ and not 1O_2 . With an increase in urea feeding, enhanced N-doping promotes O_v formation in N_y - MnO_2 . Notably, distinct triple peaks corresponding to $TEMP-^1O_2$ are evident for both N_{55} - MnO_2 and N_{25} - MnO_2 , with an intensity ratio of 1:1:1.²⁵ The intensity of the 1O_2 peak strengthens with higher O_v content, underscoring the significant role of O_v in activating O_2 . Quantitative EPR analysis indicates that N_{55} - MnO_2 generates 1O_2 at an average rate of $5.94 \text{ mol g}_{\text{cat}}^{-1} \text{ L}^{-1} \text{ min}^{-1}$ (Fig. 4c). Importantly, N_y - MnO_2 doesn't produce highly reactive hydroxyl radicals ($^{\bullet}OH$, Fig. S6†).^{51,52} To investigate the contribution of O_v to the excitation of O_2 , various ϵ - MnO_2 nanocatalysts were synthesized and characterized without N doping (Fig. S7–S9†). Interestingly, ϵ - MnO_2 -*n*-350 (where 350 indicates the thermal treatment temperature), with the highest O_s concentration of 44.4%, demonstrates the capability to generate 1O_2 under mild conditions (Fig. S10†). These findings underscore the pivotal role played by abundant surface-exposed O_v in nano-sized MnO_2 for the self-activation of O_2 . However, the catalytic activity of ϵ - MnO_2 -*n*-350 is still much lower than that of N_{55} - MnO_2 can be attributed to the doping effect of interstitial N, which will be further discussed later.

To investigate the roles of ROS in the reaction, controlled quenching experiments were conducted. As shown in Fig. 4d, the conversion of benzyl alcohol sharply decreases from >99.9% to 26% after the addition of TEMPO as a ROS quencher, indicating that ROS mediate the oxidative reaction. Upon separately introducing 1,4-benzoquinone (BQ) and isopropyl alcohol (IPA), the conversion of benzyl alcohol decreases slightly, illustrating that $^{\bullet}O_2^-$ and $^{\bullet}OH$ play subsidiary roles in the selective

oxidation process. Surprisingly, the oxidation reaction is nearly halted when furfuryl alcohol (FA) is used to capture 1O_2 . This undeniable evidence confirms 1O_2 as the primary ROS in this O_2 -mediated oxidative reaction. In summary, 1O_2 is spontaneously generated through the direct activation of O_2 , rather than the oxidation of $^{\bullet}O_2^-$ observed in photocatalytic processes.⁵² Despite O_2 being the source of ROS, the conversion of benzyl alcohol can be achieved at 31% and 25.5% under N_2 and Ar atmospheres, respectively (Fig. 4d, S11, and Table S4†). This is attributed to the involvement of O_1 in the aerobic oxidation process, following the MVK mechanism, which is consistent with previous reports.^{17,44}

Selective oxidation of alcohols

Aerobic oxidation of alcohols serves as a widely important model reaction for assessing the oxidative activity of the catalyst. However, effectively exciting O_2 with catalysts remains a challenge.^{15,20} If a catalyst can spontaneously generate 1O_2 from the ground-state oxygen, it will significantly advance the development of environmentally friendly catalysis. The plausible reaction process for efficient oxidation by N_y - MnO_2 is presented in Fig. 5. O_v and interstitial N sites promote O_2 adsorption on the surface of N_y - MnO_2 , while O_v elongate the O–O bonds, facilitating direct excitation of O_2 to 1O_2 for efficient alcohol oxidation. We evaluate the catalytic performance of N_y - MnO_2 for the aerobic oxidation of benzyl alcohol under O_2 bubbling conditions. We observe that micrometer-scale ϵ - MnO_2 displays low activity (conversion rate of 18.2% in 2.5 hours) due to its inability to activate O_2 to form 1O_2 (Fig. 6a and S10†). The C- MnO_2 exhibits negligible activity (Fig. S12 and S13†). In contrast, N_{55} - MnO_2 achieves 99.9% conversion and 99.9% selectivity in 2.5 hours, with a turnover frequency (TOF) 7.4 and 6.7 times higher than that of ϵ - MnO_2 and ϵ - MnO_2 -*n*-350, respectively (Fig. 6b and Table S5†).

To unravel the catalytic reaction mechanism, we conducted kinetics studies using various catalysts. It can be observed that the initial reaction rate remains constant under different O_2 pressures, indicating independence from O_2 pressure variations (Fig. S14 and Tables S6–S8†). Through calculation and fitting,

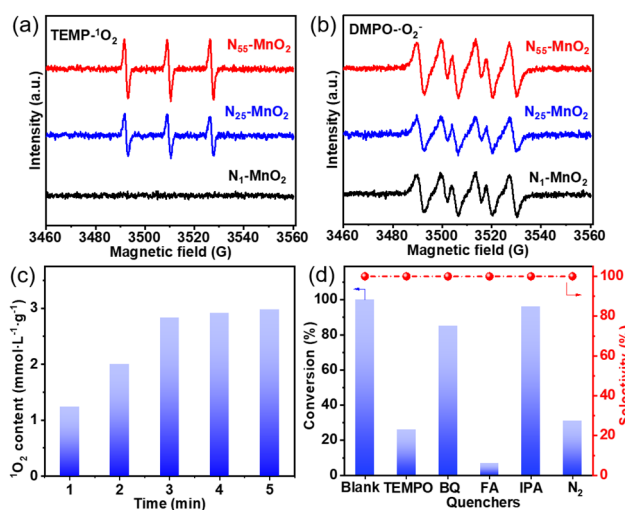


Fig. 4 The characteristic peaks of (a) $TEMP-^1O_2$ and (b) $DMPO-^{\bullet}O_2^-$ captured by EPR; (c) the content of 1O_2 produced by N_{55} - MnO_2 ; (d) the controlling experiment catalyzed by N_{55} - MnO_2 with different quenchers.

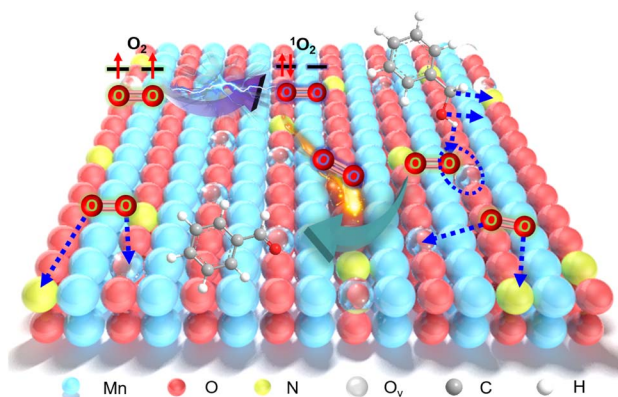


Fig. 5 Plausible reaction process for efficient oxidation by N_y - MnO_2 activating O_2 to form 1O_2 .



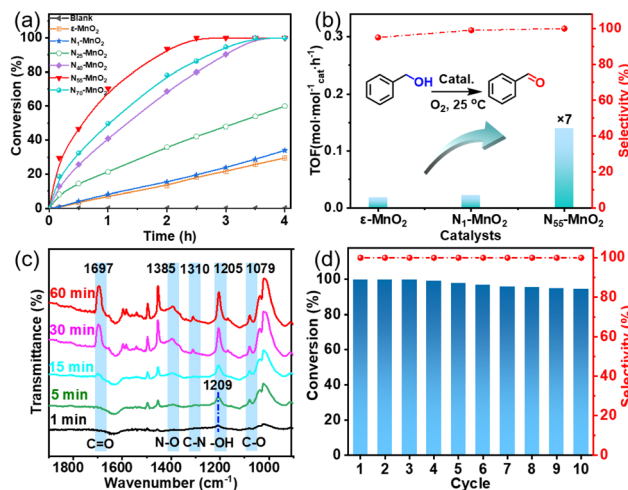


Fig. 6 (a) Aerobic oxidation of benzyl alcohol using activated ϵ -MnO₂ and N_y-MnO₂ ($y = 1, 25, 40, 55, 70$), (b) the comparison of TOF of ϵ -MnO₂, N₁-MnO₂, and N₅₅-MnO₂ (TOF = moles of benzyl alcohol converted per mole of catalyst/reaction time); (c) *in situ* IR spectra of oxidation of benzyl alcohol on the surface of N₅₅-MnO₂; (d) the recyclability of N₅₅-MnO₂ for aerobic oxidation of benzyl alcohol.

the reaction is found to be correlated with the concentration of benzyl alcohol, further demonstrating a first-order reaction (Tables S9 and S10[†]). Furthermore, we calculate the activation energies (E_a) of the N₁-MnO₂, N₂₅-MnO₂, and N₅₅-MnO₂ catalysts using the Arrhenius equation, resulting in values of 55.04 kJ mol⁻¹, 45.87 kJ mol⁻¹, and 43.17 kJ mol⁻¹, respectively (Fig. S15 and Tables S11–S13[†]). Evidently, the catalytic performance of N_y-MnO₂ is positively correlated with its O_v content, providing further evidence of the role of O_v in the oxidation process. *In situ* IR spectra were utilized to analyze the dynamic process of benzyl alcohol oxidation on the surface of N₅₅-MnO₂, revealing enhanced catalytic performance. Under an O₂ atmosphere, N₅₅-MnO₂ serves as the background for data acquisition. In the first five minutes, four characteristic peaks emerge in Fig. 6c. Compared with C-MnO₂ (Fig. S16[†]), the newly appeared N–O peak at 1385 cm⁻¹ on N₅₅-MnO₂ is attributed to O₂ adsorption by interstitial N sites. At 1310 cm⁻¹, the band corresponds to the stretching vibration of C–N bonds. The formation of C–N bonds is facilitated by the chemisorption of –OH groups from alcohol onto the interstitial N sites. After exposure to an O₂ flow for 15 minutes, the O–H band shifts from 1209 cm⁻¹ to 1205 cm⁻¹, indicating an interaction between the adsorbed O₂ species and –C–OH groups on benzyl alcohol. Continuing the exposure for 30 minutes, the broad C=O band at 1697 cm⁻¹ signifies the formation of benzyl aldehyde catalyzed by N₅₅-MnO₂.

Semiconductor catalysts have recently demonstrated an enhanced capacity for generating ¹O₂ when exposed to light, resulting in improved oxidation performance.^{24,25} In contrast, N₅₅-MnO₂ exhibits virtually unchanged activity under both light and dark conditions (Table S4[†]). This observation suggests that the inherent capability of N₅₅-MnO₂ to spontaneously generate ¹O₂ operates independently of external factors, marking

a significant difference from previously reported studies.^{25,50,53,54}

Compared to recently reported heterogeneous catalysts, the well-designed N_y-MnO₂ nanocatalysts display a unique ability to spontaneously generate sufficient ¹O₂ under mild reaction conditions. This enables the green and efficient conversion of alcohols without the need for light or additives, showcasing their superior catalytic activity (Table S14[†]).

Furthermore, we investigated the applicable substrate scope of aerobic oxidation. As shown in Table 1, aromatic primary alcohols, including benzyl alcohol and its derivatives, exhibit yields of over 99.9% for the corresponding aldehydes. Even for aromatic secondary alcohols, yields exceeding 99.9% are obtained when the reaction time extends to 6.0 hours. In comparison, the catalytic performance of N₅₅-MnO₂ in the oxidation of aliphatic alcohols (e.g., 1-hexanol) is hampered by significant

Table 1 Catalytic activity of N₅₅-MnO₂ for aerobic oxidation of various alcohols^a

Entry	Product	Conv. (%)	Sel. (%)	Yield (%)
1		99.9	>99.9	>99.9
2		99.9	>99.9	>99.9
3		99.9	>99.9	>99.9
4		82.6	>99.9	>82.6
5		99.9	>99.9	>99.9
6		99.9	>99.9	>99.9
7		99.9	>99.9	>99.9
8		99.9	>99.9	>99.9
9		99.9	>99.9	>99.9
10 ^b		99.9	>99.9	30.5
11 ^b		99.9	>99.9	47.3
12		n.d.	—	n.d.

^a Reaction condition: 5.0 mL of toluene, 0.5 mmol of alcohols, 150.0 mg of N₅₅-MnO₂, 1200 rpm, 25.0 ± 1.0 °C, O₂ flow 16.0 mL min⁻¹ 1.0 bar, reaction time 2.5 h, n. d. not detect. ^b Reaction time 6.0 h.



tests. This work used the Queensland node of the NCRIS-enabled Australian National Fabrication Facility (ANFF).

References

- C. Lu, C. Zhang, P. Wang, Y. Zhao, Y. Yang, Y. Wang, H. Yuan, S. Qu, X. Zhang, G. Song and K. Pu, *Chem*, 2020, **6**, 2314–2334.
- C. Bloyet, F. Sciortino, Y. Matsushita, P. A. Karr, A. Liyanage, W. Jevasuwan, N. Fukata, S. Maji, J. Hynek, F. D'Souza, L. K. Shrestha, K. Ariga, T. Yamazaki, N. Shirahata, J. P. Hill and D. T. Payne, *J. Am. Chem. Soc.*, 2022, **144**, 10830–10843.
- X. Bao, H. Li, Z. Wang, F. Tong, M. Liu, Z. Zheng, P. Wang, H. Cheng, Y. Liu, Y. Dai, Y. Fan, Z. Li and B. Huang, *Appl. Catal., B*, 2021, **286**, 119885.
- X. Liu, H. Yu, J. Huang, J. Su, C. Xue, X. Zhou, Y. He, Q. He, D. Xu, C. Xiong and H. Ji, *Chem. Sci.*, 2022, **13**, 9560–9568.
- D. Kalaitzakis, A. Bosveli, K. Sfakianaki, T. Montagnon and G. Vassilikogiannakis, *Angew. Chem., Int. Ed.*, 2021, **133**, 4381–4387.
- W. Wu, C. Han, Q. Zhang, Q. Zhang, Z. Li, D. J. Gosztola, G. P. Wiederrecht and M. Wu, *J. Catal.*, 2018, **361**, 222–229.
- Q. Ke, S. Fang, J. Tang, F. Li, C. Ning, Z. Tang, Q. Ling, X. Liu and P. Cui, *ChemPhotoChem*, 2022, **6**, e202200075.
- L. Kong, G. Fang, X. Xi, Y. Wen, Y. Chen, M. Xie, F. Zhu, D. Zhou and J. Zhan, *Chem. Eng. J.*, 2021, **403**, 126445.
- H. Ma, S. Long, J. Cao, F. Xu, P. Zhou, G. Zeng, X. Zhou, C. Shi, W. Sun, J. Du, K. Han, J. Fan and X. Peng, *Chem. Sci.*, 2021, **12**, 13809–13816.
- C. Lin, S. M. Bachilo and R. B. Weisman, *J. Am. Chem. Soc.*, 2020, **142**, 21189–21196.
- R. Gao, X. Mei, D. Yan, R. Liang and M. Wei, *Nat. Commun.*, 2018, **9**, 2798.
- N. Singh, P. Kumar, R. Kumar and U. Riaz, *Ind. Eng. Chem. Res.*, 2019, **58**, 14044–14057.
- Y. Chen, Z. Wang, H. Wang, J. Lu, S. Yu and H. Jiang, *J. Am. Chem. Soc.*, 2017, **139**, 2035–2044.
- R. Long, K. Mao, X. Ye, W. Yan, Y. Huang, J. Wang, Y. Fu, X. Wang, X. Wu, Y. Xie and Y. Xiong, *J. Am. Chem. Soc.*, 2013, **135**, 3200–3207.
- J. Huang, S. He, J. L. Goodsell, J. R. Mulcahy, W. Guo, A. Angerhofer and W. D. Wei, *J. Am. Chem. Soc.*, 2020, **142**, 6456–6460.
- W. Zhang, W. Huang, J. Jin, Y. Gan and S. Zhang, *Appl. Catal., B*, 2021, **292**, 120197.
- J. Tang, Y. Cao, F. Ruan, F. Li, Y. Jin, M. N. Ha, X. Han and Q. Ke, *Ind. Eng. Chem. Res.*, 2020, **59**, 9408–9413.
- J. Chen, H. Tang, M. Huang, Y. Yan, J. Zhang, H. Liu, J. Zhang, G. Wang and R. Wang, *ACS Appl. Mater. Interfaces*, 2021, **13**, 26960–26970.
- F. Ruan, F. Li, Z. Dong, Q. Ke, Y. Jin, W. Zhan, M. N. Ha and J. Tang, *Green Synth. Catal.*, 2021, **2**, 38–44.
- M. Koutani, E. Hayashi, K. Kamata and M. Hara, *J. Am. Chem. Soc.*, 2022, **144**, 14090–14100.
- Q. Ke, Y. Jin, F. Ruan, M. N. Ha, D. Li, P. Cui, Y. Cao, H. Wang, T. Wang, V. N. Nguyen, X. Han, X. Wang and P. Cui, *Green Chem.*, 2019, **21**, 4313–4318.
- Y. Pérez-Badell, X. Solans-Monfort, M. Sodupe and L. A. Montero, *Phys. Chem. Chem. Phys.*, 2010, **12**, 442–452.
- J. Oviedo and M. J. Gillan, *Surf. Sci.*, 2001, **490**, 221–236.
- Y. Hao, B. Liu, L. Tian, F. Li, J. Ren, S. Liu, Y. Liu, J. Zhao and X. Wang, *ACS Appl. Mater. Interfaces*, 2017, **9**, 12687–12693.
- J. Wang, X. Xu, Y. Liu, Z. Wang, P. Wang, Z. Zheng, H. Cheng, Y. Dai and B. Huang, *ChemSusChem*, 2020, **13**, 3488–3494.
- S. Tan, Y. Ji, Y. Zhao, A. Zhao, B. Wang, J. Yang and J. G. Hou, *J. Am. Chem. Soc.*, 2011, **133**, 2002–2009.
- M. Setvín, U. Aschauer, P. Scheiber, Y. Li, W. Hou, M. Schmid, A. Selloni and U. Diebold, *Science*, 2013, **341**, 988–991.
- M. Li, S. You, X. Duan and Y. Liu, *Appl. Catal., B*, 2022, **312**, 121419.
- X. Kang, G. Dong and T. Dong, *ACS Appl. Energy Mater.*, 2023, **6**, 1025–1036.
- Y. Zhuo, X. Guo, W. Cai, T. Shao, D. Xia, C. Li and S. Liu, *Appl. Catal., B*, 2023, **333**, 122789.
- M. Yang, K. Wu, S. Sun, J. Duan, X. Liu, J. Cui, S. Liang and Y. Ren, *ACS Catal.*, 2023, **13**, 681–691.
- J. Tang, Q. Zhang, K. Hu, P. Zhang and J. Wang, *J. Catal.*, 2017, **353**, 192–198.
- M. Liu, Q. Wang, Z. Liu, Y. Zhao, X. Lai, J. Bi and D. Gao, *Chem. Eng. J.*, 2020, **383**, 123161.
- P. V. Vardhan, M. B. Idris, H. Y. Liu, S. R. Sivakkumar, P. Balaya and S. Devaraj, *J. Electrochem. Soc.*, 2018, **165**, A1865.
- T. He, X. Zeng and S. Rong, *J. Mater. Chem. A*, 2020, **8**, 8383–8396.
- T. J. Frankcombe and Y. Liu, *Chem. Mater.*, 2023, **35**, 5468–5474.
- G. Qi, X. Liu, C. Li, C. Wang and Z. Yuan, *Angew. Chem., Int. Ed.*, 2019, **58**, 17406–17411.
- L. Liu, R. Liu, T. Xu, Q. Zhang, Y. Tan, Q. Zhang, J. Ding and Y. Tang, *Inorg. Chem.*, 2020, **59**, 14407–14414.
- S. Rong, K. Li, P. Zhang, F. Liu and J. Zhang, *Catal. Sci. Technol.*, 2018, **8**, 1799–1812.
- Y. Huang, Y. Liu, W. Wang, M. Chen, H. Li, S. Lee, W. Ho, T. Huang and J. Cao, *Appl. Catal., B*, 2020, **278**, 119294.
- F. Morales, D. Grandjean, A. Mens, F. M. F. Groot and B. M. Weckhuysen, *J. Phys. Chem. B*, 2006, **110**, 8626–8639.
- Y. Xu, J. Dhainaut, G. Rochard, J. Dacquain, A. Mamede, J. Giraudon, J. Lamonier, H. Zhang and S. Royer, *Chem. Eng. J.*, 2020, **388**, 124146.
- J. Tang, B. Jiao, W. Chen, F. Ruan, F. Li, P. Cui, C. Wan, M. N. Ha, V. N. Nguyen and Q. Ke, *Nano Res.*, 2022, **15**, 6076–6083.
- Y. Jin, F. Li, P. Cui, Y. Yang, Q. Ke, M. N. Ha, W. Zhan, F. Ruan, C. Wan, Z. Lei, V. N. Nguyen, W. Chen and J. Tang, *Nano Res.*, 2021, **14**, 2637–2643.
- Q. Ke, D. Yi, Y. Jin, F. Lu, B. Zhou, F. Zhan, Y. Yang, D. Gao, P. Yan, C. Wan, P. Cui, D. Golberg, J. Yao and X. Wang, *ACS Sustain. Chem. Eng.*, 2020, **8**, 5734–5741.



- 46 H. Li, Y. Zhang, J. Tang, G. Huang, P. Cui and Q. Ke, *Green Synth. Catal.*, 2022, DOI: [10.1016/j.gresc.2022.09.005](https://doi.org/10.1016/j.gresc.2022.09.005).
- 47 J. Yu, T. Zeng, H. Wang, H. Zhang, Y. Sun, L. Chen, S. Song, L. Li and H. Shi, *Chem. Eng. J.*, 2020, **394**, 124458.
- 48 H. Li, J. Shang, Z. Ai and L. Zhang, *J. Am. Chem. Soc.*, 2015, **137**, 6393–6399.
- 49 Y. Lin, Z. Liu, L. Yu, G. Zhang, H. Tan, K. Wu, F. Song, A. K. Mechler, P. P. M. Schleker, Q. Lu, B. Zhang and S. Heumann, *Angew. Chem., Int. Ed.*, 2021, **60**, 3299–3306.
- 50 F. Li, J. Tang, Q. Ke, Y. Guo, M. N. Ha, C. Wan, Z. Lei, J. Gu, Q. Ling, V. N. Nguyen and W. Zhan, *ACS Catal.*, 2021, **11**, 11855–11866.
- 51 J. Li, X. Wang, J. Tian, X. Zhang and F. Shi, *Rare Met.*, 2023, **42**, 1877–1887.
- 52 B. He, H. Jin, Y. Wang, C. Fan, Y. Wang, X. Zhang, J. Liu, R. Li and J. Liu, *Rare Met.*, 2022, **41**, 132–143.
- 53 N. Siemer, A. Lüken, M. Zalibera, J. Frenzel, D. Muñoz-Santiburcio, A. Savitsky, W. Lubitz, M. Muhler, D. Marx and J. Strunk, *J. Am. Chem. Soc.*, 2018, **140**, 18082–18092.
- 54 T. Xia, W. Gong, Y. Chen, M. Duan, J. Ma, X. Cui, Y. Dai, C. Gao and Y. Xiong, *Angew. Chem., Int. Ed.*, 2022, **61**, e202204225.

